Algorithms and Analyses for Joint Spectral Image Reconstruction in Y-90 Bremsstrahlung SPECT

Se Young Chun, *Member, IEEE*, Minh Phuong Nguyen, Thanh Quoc Phan, Hanvit Kim, *Student Member, IEEE*, Jeffrey A. Fessler, *Fellow, IEEE*, and Yuni K. Dewaraja, *Member, IEEE*

***Abstract*— Quantitative yttrium-90 (Y-90) SPECT imaging is challenging due to the nature of Y-90, an almost pure beta emitter that is associated with a continuous spectrum of bremsstrahlung photons that have a relatively low yield. This paper proposes joint spectral reconstruction (JSR), a novel bremsstrahlung SPECT reconstruction method that uses multiple narrow acquisition windows with accurate multi-band forward modeling to cover a wide range of the energy spectrum. Theoretical analyses using Fisher information and Monte-Carlo (MC) simulation with a digital phantom show that the proposed JSR model with multiple acquisition windows has better performance in terms of covariance (precision) than previous methods using multi-band forward modeling with a single acquisition window, or using a single-band forward modeling with a single acquisition window. We also propose an energy-window subset (ES) algorithm for JSR to achieve fast empirical convergence and maximum-likelihood based initialization for all reconstruction methods to improve quantification accuracy in early iterations. For both MC simulation with a digital phantom and experimental study with a physical multi-sphere phantom, our proposed JSR-ES, a fast algorithm for JSR with ES, yielded higher recovery coefficients (RCs) on hot spheres over all iterations and sphere sizes than all the other evaluated methods, due to fast empirical convergence. In experimental study, for the smallest hot sphere (diameter 1.6cm), at the 20th iteration the increase in RCs with JSR-ES was 66 and 31% compared with single wide and narrow band forward models, respectively. JSR-ES also yielded lower residual count error (RCE) on a cold sphere over all iterations than other methods for MC simulation with known scatter, but led to greater RCE compared with single narrow band forward model at higher iterations for experimental study when using estimated scatter.**

***Index Terms*— Y-90, SPECT, joint spectral reconstruction, bremsstrahlung, energy-window subset.**

Manuscript received August 27, 2019; revised October 11, 2019; accepted October 17, 2019. Date of publication October 23, 2019; date of current version April 30, 2020. This work was supported in part by the Basic Science Research Program under the National Research Foundation of Korea (NRF) through the Ministry of Education under Grant NRF-2017R1D1A1B05035810, in part by the National Research Foundation of Korea (NRF) through the Korean Government, Ministry of Science and ICT (MSIT), under Grant NRF-2014R1A1A1007928, and in part by the National Institute of Biomedical Imaging and Bioengineering, National Institute of Health, U.S. Department of Health and Human Services under Grant R01 EB022075. *(Corresponding author: Se Young Chun.)*

S. Y. Chun and H. Kim are with the Department of Electrical Engineering (EE), Ulsan National Institute of Science and Technology (UNIST), Ulsan 44919, South Korea (e-mail: sychun@unist.ac.kr).

M. P. Nguyen was with the Department of Electrical Engineering (EE), Ulsan National Institute of Science and Technology (UNIST), Ulsan 44919, South Korea. He is now with the Section Biomedical Imaging, Delft University of Technology, 2628 Delft, The Netherlands.

T. Q. Phan was with the Department of Electrical Engineering (EE), Ulsan National Institute of Science and Technology (UNIST), Ulsan 44919, South Korea. He is now with the Department of Biomedical Engineering, The Catholic University of America, Washington, DC 20064 USA.

J. A. Fessler is with the Department of Electrical Engineering and Computer Science, University of Michigan, Ann Arbor, MI 48109 USA.

Y. K. Dewaraja is with the Department of Radiology, University of Michigan, Ann Arbor, MI 48109 USA.

Color versions of one or more of the figures in this article are available online at http://ieeexplore.ieee.org.

Digital Object Identifier 10.1109/TMI.2019.2949068

I. Introduction

INTERNAL emitter therapies with Y-90 have yielded promising clinical results in innovative cancer treatments such as radioembolization for nonresectable liver tumors [1], [2], radioimmunotherapy for non-Hodgkin's lymphoma [3] and peptide receptor radionuclide therapy for neuroendocrine tumors [4]. Post-therapy quantitative Y-90 PET and SPECT imaging allows confirmation of the delivered absorbed doses to lesions and normal organs for early assessment of efficacy and toxicity and implementation of further treatment when needed. Despite the superior spatial resolution and quantitative accuracy of PET, there is considerable interest in Y-90 imaging by SPECT because of the wider availability and lower cost associated with SPECT.

SPECT imaging of Y-90 is challenging because it is an almost pure beta emitter that has to be imaged via the associated bremsstrahlung photons that have a continuous energy spectrum (Fig. 1) extending to 2.3 MeV [5]. In addition to the complexities of imaging photons that have a continuous energy spectrum, bremsstrahlung photon generation in tissue is an inefficient process with $<5\%$ of beta interactions yielding imageable photons of >50 keV [6]. Because of this low yield, it is desirable to include as many photons as possible in the

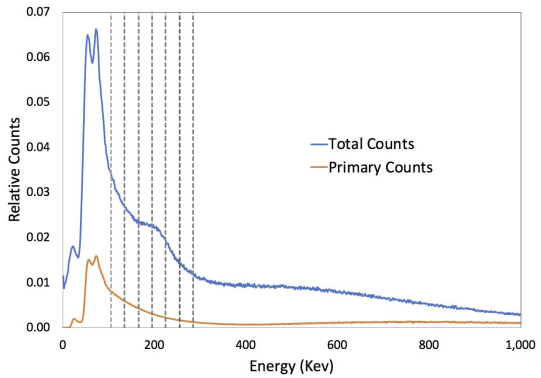

Fig. 1. Y-90 bremsstrahlung energy spectrum corresponding to the sphere phantom MC simulation of the current study. The total spectrum and primary (un-scattered photons) components are shown. A lower energy cutoff of 50 keV was used. The six 30 keV narrow windows (over 105-285 keV range) used for JSR are indicated in vertical dashed lines. Single wide and narrow band forward models correspond to single windows covering the range of 105-135 keV and 105-285 keV, respectively.

acquisition. However, the wide bremsstrahlung spectrum has been underutilized in some past studies with reconstruction performed using a relatively narrow energy band [5], [7], [8].

There have been studies on improving quantitative Y-90 SPECT by dealing with continuous energy ranges in the image reconstruction model. One approach is to model the continuous energy spectrum in the forward (and backward) projectors of iterative reconstructions. Rong *et al.* proposed MER (multienergy range) that incorporated energy-dependent collimator-detector responses (CDRs), attenuation correction factors, and scatter kernels (ESSE) for 4 energy bands (0-250, 250-500, 500-1000, 1000-2000 keV) with a single energy window acquisition (0-500 keV) [9]. Monte-Carlo (MC) simulations for a point source or a cylinder were used to estimate CDRs, attenuations and scatter kernels. Yue *et al.* later showed that the MER SPECT reconstruction method yielded comparable results to Y-90 PET-CT in terms of estimating total activity in the liver and activity distributions within treated volumes [10]. However, MER did not take patient dependent, detailed and accurate photon transport physics into account and used unmatched forward and backward projectors that may cause convergence issues with some iterative algorithms. Elschot *et al.* proposed a method that is similar to MER, but replaces MER's pre-calculated forward projector with a fast MC simulator for more accurate forward modeling with 8 energy bands (50-64, 64-94, 94-149, 149-250, 250-373, 373-607, 607-1044, 1044-2000 keV) with a single acquisition window (50-250 keV) [11]. Even though it yielded promising results that are comparable to time-of-flight PET imaging, the proposed method had to perform MC simulations every iteration that could be in general slower than using pre-calculated kernels such as [9] or hypothetically more computationally intensive than the approaches that use MC simulations every 5 iterations for scatter estimation (*e.g.*, [8]) assuming the same MC simulator used. However, note that unlike SIMIND [12] that was used in our MC simulations, the work of [11] made several approximations for the collimator so that the simulation time could be reduced. Lastly, it is not straightforward to implement the matched backward projector for the MC forward projector. Rong's and Elschot's methods look different, but both of them were based on the multi-band forward model with a single acquisition window (denoted by SSR-WA).

TABLE I
ALL EVALUATED RECONSTRUCTION METHODS USED OSEM WITH 4 ORDERED SUBSETS. JSR-ES USED ADDITIONAL 3 ENERGY SUBSETS

Abbrev.	Description
SSR-N	single-band acquisition, single-band model, 105-135 keV
SSR-W	single-band acquisition, single-band model, 105-285 keV
SSR-WA	single-band acquisition, multi-band model, 105-285 keV
JSR	multi-band acquisition, multi-band model, 105-285 keV
JSR-ES	the same as JSR plus energy-window subset algorithm

Recently, we proposed a joint spectral reconstruction (JSR) that uses multi-band forward model with multi-band measurements [13] to use more of the available photons and to exploit the availability of multi-window, list-mode SPECT acquisition systems. However, there are still remaining challenges.

Firstly, there has been no comparison study among different reconstruction methods such as [8], [9], [11], [13]. Since there are too many reconstruction parameters and methods to be optimized (*e.g.*, energy windows, iterations, subsets, scatters), fair experimental comparisons are challenging. This paper attempts to analyze and compare theoretical performances using Fisher information of the various methods.

Secondly, JSR was relatively slow compared to the method with a single-band forward model and a single-band acquisition (we will denote it by SSR-N for a narrow energy window and by SSR-W for a wide window). Ordered-subset (OS) algorithm is a typical method to speed up empirical convergence by utilizing angular subsets for gradient approximations. In a similar way, we propose to include energy-window subsetting (ES), along with conventional angular subsetting (OS), for gradient approximations to achieve faster convergence.

Lastly, we investigated a principled method to determine a good initial image using maximum-likelihood (ML) to improve quantification accuracy in early iterations. We use both simulations and a physical phantom scan to evaluate our proposed methods. Note that for the methods evaluated in the current work, the scatter estimate is generated by MC simulation and is updated every 5 iterations. By including the MC scatter estimate as an additive term in the forward model, our reconstruction method is able to use matched projectors. All methods are summarized in Table I.

II. BACKGROUND

A. Single Spectral Reconstruction With Single Energy Window

For a given Y-90 distribution in the body, there are certain bremsstrahlung photons associated with the Y-90 beta decay that are emitted within any given energy window and only some of which are recorded by the detector. Define $\mathbf{x}_e \in \mathbb{R}^N$ (in units of counts) as emitted "primary" (the desired un-scattered) bremsstrahlung photons within the energy range

of the eth energy window that are recorded by the detector. Let $\mathbf{y}_e \in \mathbb{R}^M$ be a total measured projection and $\mathbf{s}_e \in \mathbb{R}^M$ denote the (ensemble mean) scatter projection for the eth energy window. Define $\mathbf{A}_e \in \mathbb{R}^{M\times N}$ to be a forward model for the eth energy window that maps from the emitted primary photons to the detectors including energy-dependent attenuation information and CDR [14]. Then, the measurement model is

$$\mathbf{y}_e \sim \text{Poisson}(\bar{\mathbf{y}}_e), \quad \bar{\mathbf{y}}_e := \mathbf{A}_e\mathbf{x}_e + \mathbf{s}_e \tag{1}$$

where Poisson$(\cdot)$ is a component-wise, independent Poisson distribution.

If one estimates the scatter contribution $\mathbf{s}_e$ via MC methods [12], then for SSR-N and SSR-W, the goal is to reconstruct the unknown emitted counts $\mathbf{x}_e$ from the measurement $\mathbf{y}_e$. The maximum likelihood (ML) estimate of $\mathbf{x}_e$ is:

$$\hat{\mathbf{x}}_e := \arg\max_{\mathbf{x}_e \succeq \mathbf{0}} \text{L}(\mathbf{x}_e; \mathbf{A}_e, \mathbf{y}_e, \mathbf{s}_e) \tag{2}$$

where $\mathbf{x}_e \succeq \mathbf{0}$ implies the non-negativity constraint on $\mathbf{x}_e$ and $\text{L}(\cdot, \cdot; \mathbf{A}_e, \mathbf{y}_e, \mathbf{s}_e)$ is the sum of Poisson log-likelihoods:

$$\text{L}(\mathbf{x}_e; \mathbf{A}_e, \mathbf{y}_e, \mathbf{s}_e) := \mathbf{1}_M'(\mathbf{y}_e \odot \log \bar{\mathbf{y}}_e - \bar{\mathbf{y}}_e)$$

where $\mathbf{1}_M$ is a vector whose elements are all one with the length of M, $'$ is a transpose operator, log is an element-wise log function, and $\odot$ is a component-wise multiplication (Hadamard product). A popular algorithm for solving (2) is maximum likelihood expectation maximization (ML-EM) [15]:

$$\hat{\mathbf{x}}_e^{(n+1)} = \hat{\mathbf{x}}_e^{(n)} + \hat{\mathbf{x}}_e^{(n)} \oslash \mathbf{a}_e \odot \nabla \text{L}(\hat{\mathbf{x}}_e^{(n)}; \mathbf{A}_e, \mathbf{y}_e, \mathbf{s}_e) \tag{3}$$

where $\hat{\mathbf{x}}_e^{(n)}$ is an estimate at the nth iteration, $\oslash$ is a component-wise division (Hadamard division), $\mathbf{a}_e := \mathbf{A}_e{}'\mathbf{1}_M$ is a sensitivity image for $\mathbf{A}_e$, and

$$\nabla \text{L}(\hat{\mathbf{x}}_e^{(n)}; \mathbf{A}_e, \mathbf{y}_e, \mathbf{s}_e) = \mathbf{A}_e'(\mathbf{y}_e \oslash \bar{\mathbf{y}}_e^{(n)} - \mathbf{1}_M)$$

where $\bar{\mathbf{y}}_e^{(n)} := \mathbf{A}_e\hat{\mathbf{x}}_e^{(n)} + \mathbf{s}_e$.

One can accelerate convergence by using ordered-subset (OS) approach (ML-OSEM) [16] so that the next estimate (either $\hat{\mathbf{x}}_e^{(n,k+1)}$ or $\hat{\mathbf{x}}_e^{(n+1,1)}$) becomes

$$\hat{\mathbf{x}}_e^{(n,k)} + \hat{\mathbf{x}}_e^{(n,k)} \oslash \mathbf{a}_{e,k} \odot \nabla \text{L}(\hat{\mathbf{x}}_e^{(n,k)}; \mathbf{A}_{e,k}, \mathbf{y}_{e,k}, \mathbf{s}_{e,k}) \tag{4}$$

where $k = 1, \ldots, K$ is an index for Ω_k that is a subset of all measurement indices $1, \ldots, M$, $\mathbf{a}_{e,k} := \mathbf{A}_{e,k}{}'\mathbf{1}_K$, $\mathbf{A}_{e,k} \in \mathbb{R}^{K\times N}$ is a sub-matrix to collect the rows of $\mathbf{A}_e$ corresponding to the index subset Ω_k, and $\mathbf{y}_{e,k}, \mathbf{s}_{e,k}$ are vectors to collect the elements of $\mathbf{y}_e, \mathbf{s}_e$ corresponding to Ω_k, respectively.

B. Model Accuracy vs. Noise Property Trade-Off in SSR

The model (1) and its corresponding algorithm (4) can be used for SSR-N and SSR-W (later SSR-WA, too) by changing its forward projection model $\mathbf{A}_e$, measurement $\mathbf{y}_e$, and scatter information $\mathbf{s}_e$. For example, with a narrow single energy window of 105-135 keV, $\mathbf{A}_e$ could be more accurately modeling the energy-dependent CDR and attenuation correction information than that with a wide single energy window (*e.g.*, 105-285 keV). However, due to the narrow acquisition window, $\mathbf{y}_e$ will have fewer counts (be more noisy) than that with a wide single energy window.

In this work, we divided a wide energy window into 6 narrow windows indicated in Fig. 1 (105-135, 135-165, 165-195, 195-225, 225-255, 255-285 keV) where the indices for energy windows are $e = 1, \ldots, 6$. Note that lower energies were not included in order to avoid lead x-rays. We will denote the reconstruction result $\hat{\mathbf{x}}_1^{(n,k)}$ of the first narrow energy window "single spectral reconstruction with narrow energy window (SSR-N)." Note that the first narrow energy window contains the highest fraction of primary counts (ratio of un-scattered to total counts) among all 6 windows.

One can also apply "single" spectral reconstruction for a wide energy window (e.g., 105-285 keV) as follows:

$$\hat{\mathbf{x}}_W^{(n+1)} = \hat{\mathbf{x}}_W^{(n)} + \hat{\mathbf{x}}_W^{(n)} \oslash \mathbf{a}_W \odot \nabla \text{L}(\hat{\mathbf{x}}_W^{(n)}; \mathbf{A}_W, \mathbf{y}_W, \mathbf{s}_W) \tag{5}$$

where $\mathbf{a}_W := \mathbf{A}_W{}'\mathbf{1}_M$ and $\mathbf{A}_W, \mathbf{y}_W, \mathbf{s}_W$ are forward model, measurement vector, known scatter for the wide energy window (e.g., 105-285 keV), respectively. OS approximation can also be done in a similar manner as (4). Due to wide energy window, $\mathbf{y}_W, \mathbf{s}_W$ will have high counts to reduce noise level in the reconstructed image $\hat{\mathbf{x}}_W^{(n)}$, but the accuracy of modeling $\mathbf{A}_W$ will be decreased because of the energy dependence of attenuation and CDR. We will denote this reconstruction "single spectral reconstruction with wide energy window (SSR-W)." Note that the relationships between SSR-N and SSR-W are $\mathbf{y}_W = \sum_e \mathbf{y}_e$ and $\mathbf{s}_W = \sum_e \mathbf{s}_e$ with different forward models $\mathbf{A}_e$ (more accurate) and $\mathbf{A}_W$ (less accurate).

III. Methods

A. Emitted Photon Model in Multiple Energy Windows

Consider the total emitted bremsstrahlung photons $\mathbf{x}$. Then, for the emitted photons $\mathbf{x}_e$ in the eth energy window, the following relationship holds:

$$\mathbf{x} = \sum_e \mathbf{x}_e. \tag{6}$$

We further modeled the emitted bremsstrahlung photons $\mathbf{x}_e$ as proportional to the total emitted photons $\mathbf{x}$ for direct, simplified representations as follows:

$$\mathbf{x}_e = \tau_e\mathbf{x} \tag{7}$$

where τ_e is a scale parameter describing the ratio of emitted photons in the eth energy window to total emitted photons in all energy ranges with $\sum_e \tau_e = 1$. One can estimate all τ_e's by measuring primary counts $\mathbf{y}_e - \mathbf{s}_e$ in each energy window [13] or by a simple MC simulation with a point source [17]. Note that (7) does not imply $\mathbf{y}_e = \tau_e\mathbf{y}$ due to energy-dependent forward model $\mathbf{A}_e$ and energy-dependent scatter $\mathbf{s}_e$.

B. Joint Spectral Reconstruction With Multiple Energy Windows

By combining the forward model for a single energy window (1) and our emitted bremsstrahlung photon model for multiple energy windows (7), we can stack up all forward

models for multiple energy windows to create a joint forward model as follows [13]:

$$\mathbf{y}_J \sim \text{Poisson}\left(\mathbf{A}_J\mathbf{x} + \mathbf{s}_J\right) \tag{8}$$

where $\mathbf{y}_J$, $\mathbf{A}_J$, $\mathbf{s}_J$ are stacks of $\mathbf{y}_e$, $\mathbf{A}_e\tau_e$, $\mathbf{s}_e$ for all e, respectively, or

$$\mathbf{y}_J := \begin{bmatrix} \vdots \\ \mathbf{y}_e \\ \vdots \end{bmatrix}, \quad \mathbf{A}_J := \begin{bmatrix} \vdots \\ \mathbf{A}_e\tau_e \\ \vdots \end{bmatrix}, \quad \mathbf{s}_J := \begin{bmatrix} \vdots \\ \mathbf{s}_e \\ \vdots \end{bmatrix}.$$

Using E energy windows, a ML-EM algorithm for (8) is

$$\hat{\mathbf{x}}^{(n+1)} = \hat{\mathbf{x}}^{(n)} + \hat{\mathbf{x}}^{(n)} \oslash \mathbf{a}_J \odot \nabla \mathrm{L}(\hat{\mathbf{x}}^{(n)}; \mathbf{A}_J, \mathbf{y}_J, \mathbf{s}_J) \tag{9}$$

where $\hat{\mathbf{x}}^{(n)}$ is an estimate at the nth iteration, $\mathbf{a}_J := \mathbf{A}_J{}'\mathbf{1}_{ME}$ is a sensitivity image for $\mathbf{A}_J$, and

$$\nabla \mathrm{L}(\hat{\mathbf{x}}^{(n)}; \mathbf{A}_J, \mathbf{y}_J, \mathbf{s}_J) = \mathbf{A}'_J(\mathbf{y}_J \oslash \bar{\mathbf{y}}_J^{(n)} - \mathbf{1}_{ME})$$

where $\bar{\mathbf{y}}_J^{(n)} := \mathbf{A}_J\hat{\mathbf{x}}^{(n)} + \mathbf{s}_J$. The natural ML-OSEM for (9) partitions the data into K sets of view angles and the next estimate (either $\hat{\mathbf{x}}^{(n,k+1)}$ or $\hat{\mathbf{x}}^{(n+1,1)}$) will be

$$\hat{\mathbf{x}}^{(n,k)} + \hat{\mathbf{x}}^{(n,k)} \oslash \mathbf{a}_{J,k} \odot \nabla \mathrm{L}(\hat{\mathbf{x}}^{(n,k)}; \mathbf{A}_{J,k}, \mathbf{y}_{J,k}, \mathbf{s}_{J,k}),$$
$$\mathbf{y}_{J,k} := \begin{bmatrix} \vdots \\ \mathbf{y}_{e,k} \\ \vdots \end{bmatrix}, \quad \mathbf{A}_{J,k} := \begin{bmatrix} \vdots \\ \mathbf{A}_{e,k}\tau_e \\ \vdots \end{bmatrix}, \quad \mathbf{s}_{J,k} := \begin{bmatrix} \vdots \\ \mathbf{s}_{e,k} \\ \vdots \end{bmatrix} \tag{10}$$

and $\mathbf{a}_{J,k} := \mathbf{A}_{J,k}{}'\mathbf{1}_{ME/K}$. Note that the number of rows in $\mathbf{A}_{J,k}$ is K times smaller than the number of rows in $\mathbf{A}_J$. We call these algorithms "joint spectral reconstruction with multiple energy windows (JSR)."

C. Energy-Window Subset (ES) Approximation

The OS approach significantly improved the speed of empirical convergence in ML-EM [16] by approximating the gradient of the cost function with partial measurements in the subset of projection angles. For example, the OS version of SSR-N uses the following approximation:

$$\mathbf{A}'_e(\mathbf{y}_e \oslash \bar{\mathbf{y}}_e^{(n)} - \mathbf{1}_M) \approx K\mathbf{A}'_{e,k}(\mathbf{y}_{e,k} \oslash \bar{\mathbf{y}}_{e,k}^{(n)} - \mathbf{1}_{M/K})$$

where $\bar{\mathbf{y}}_e^{(n)} := \mathbf{A}_e\hat{\mathbf{x}}_e^{(n)} + \mathbf{s}_e$ and $\bar{\mathbf{y}}_{e,k}^{(n)} := \mathbf{A}_{e,k}\hat{\mathbf{x}}_e^{(n)} + \mathbf{s}_{e,k}$. For (8), ML-OSEM uses the following gradient approximation:

$$\mathbf{A}'_J(\mathbf{y}_J \oslash \bar{\mathbf{y}}_J^{(n)} - \mathbf{1}_{ME}) \approx K\mathbf{A}'_{J,k}(\mathbf{y}_{J,k} \oslash \bar{\mathbf{y}}_{J,k}^{(n)} - \mathbf{1}_{ME/K})$$

where $\bar{\mathbf{y}}_J^{(n)} := \mathbf{A}_J\hat{\mathbf{x}}^{(n)} + \mathbf{s}_J$ and $\bar{\mathbf{y}}_{J,k}^{(n)} := \mathbf{A}_{J,k}\hat{\mathbf{x}}^{(n)} + \mathbf{s}_{J,k}$. Even though it may be possible to share computations for ray tracing among different energy windows, it is still unavoidable to increase computation complexity due to multiple energy windows and forward models with E times more measurements for each gradient computation.

Assuming that the model (7) is accurate, we propose an energy-window subset (ES) approximation for OS-type gradient computations. First of all, we divide energy windows into L energy-window subsets where each subset contains one or more energy windows. In other words, the lth energy subset contains all energy window indices e such that $e \in \Lambda_l$. Then, the proposed gradient approximation using ES is as follows:

$$\mathbf{A}'_J(\mathbf{y}_J \oslash \bar{\mathbf{y}}_J^{(n)} - \mathbf{1}_{ME}) \approx LK\mathbf{A}'_{J,l,k}(\mathbf{y}_{J,l,k} \oslash \bar{\mathbf{y}}_{J,l,k}^{(n)} - \mathbf{1}_{ME/KL})$$

where $\bar{\mathbf{y}}_{J,l,k}^{(n)} := \mathbf{A}_{J,l,k}\hat{\mathbf{x}}^{(n)} + \mathbf{s}_{J,l,k}$, $\mathbf{y}_{J,l,k}$ is a stack of $\mathbf{y}_{e,k}$ for all $e \in \Lambda_l$, $\mathbf{A}_{J,l,k}$ is a stack of $\mathbf{A}_{e,k}\tau_e$ for all $e \in \Lambda_l$, and $\mathbf{s}_{J,l,k}$ is a stack of $\mathbf{s}_{e,k}$ for all $e \in \Lambda_l$.

We empirically found that it is advantageous to divide energy windows into subsets so that each subset contains similar number of counts. For our 6 narrow energy windows in Fig. 1, we used 3 energy subsets where the first group contains 105-135 keV window, the second group contains 135-165 and 225-255 keV windows, and the last subset contains the rest. Note that ES is used along with conventional OS, thus 3 times more subsets will be used when using ES approximation.

D. Maximum Likelihood-Based Initialization

Theoretically, ML-EM in (3), (5), (9) and ML-OSEM in (4), (10) require an initial image with positive values. In practice, a uniform image with a very small positive value ϵ or an image with the support from an attenuation image is used as an initialization image. We next propose a principled way of choosing an initialization image, called ML-based initialization, by modifying the latter approach.

Consider an image with the support from an attenuation image, denoted by $\mathbf{m}$. Then, we model our initial image as

$$\hat{\mathbf{x}}_e^{(0)} = c\mathbf{m} \tag{11}$$

where c is a unknown positive real number. By plugging this model into any cost function that we are optimizing, we can change a high dimensional optimization problem of (2) into a 1D optimization problem for the scaling factor c as follows:

$$\hat{c} := \arg\max_{c>0} \mathrm{L}(c\mathbf{m}; \mathbf{A}_e, \mathbf{y}_e, \mathbf{s}_e). \tag{12}$$

This maximization only requires one forward projection of $\mathbf{m}$ and a simple 1D optimization algorithm. It can be extended to JSR or other likelihood based image reconstructions easily. In our simulation studies for bremsstrahlung SPECT, we observed that it was important to choose a reasonable value c for good performance of image reconstructions in early iterations and our proposed method provided an effective method for it.

IV. Noise Property Analysis

A. Single Spectral Reconstruction With Accurate Forward Model

There have been studies for Y-90 SPECT image reconstruction using multi-band forward models with a single-band acquisition window [9], [11], [18]. Mathematically, these approaches are approximately based on the following model:

$$\mathbf{y}_W \sim \text{Poisson}\left(\mathbf{A}_S\mathbf{x} + \mathbf{s}_W\right) \tag{13}$$

where $\mathbf{y}_W = \sum_e \mathbf{y}_e$, $\mathbf{A}_S = \sum_e \mathbf{A}_e\tau_e$, and $\mathbf{s}_W = \sum_e \mathbf{s}_e$. This new forward model $\mathbf{A}_S$ allows to have a wide energy window for more counts while maintaining the same accuracy in the

forward model as $\mathbf{A}_e$ for all e in (1). Based on (13), a ML-EM algorithm can be derived as follows:

$$\hat{\mathbf{x}}_S^{(n+1)} = \hat{\mathbf{x}}_S^{(n)} + \hat{\mathbf{x}}_S^{(n)} \oslash \mathbf{a}_S \odot \nabla \mathrm{L}(\hat{\mathbf{x}}_S^{(n)}; \mathbf{A}_S, \mathbf{y}_W, \mathbf{s}_W). \quad (14)$$

It is trivial to extend this update (14) to ML-OSEM to speed up convergence rate by using $\mathbf{A}_{S,k} = \sum_e \mathbf{A}_{e,k}\tau_e$ instead of $\mathbf{A}_S$. However, applying our proposed ES approximation does not seem feasible since it is not trivial to decompose $\mathbf{y}_W$ into $\mathbf{y}_e$'s. We denote this method by SSR-WA.

B. Theoretical Precision Limits of SSR-N, SSR-WA and JSR

The precision of an unbiased estimator is bounded below by the inverse of the Fisher information matrix. Consider a random vector $\mathbf{V}$ and its realization $\mathbf{v}$. Let $f_{\boldsymbol{\theta}}(\mathbf{v})$ denote a family of densities of $\mathbf{V}$ parameterized by $\boldsymbol{\theta}$. Then, the Fisher information matrix for $\mathbf{V}$ is defined as follows:

$$\mathbf{J}(\mathbf{V}; \boldsymbol{\theta}) := \mathrm{Cov}\left\{\nabla_{\boldsymbol{\theta}} \log f_{\boldsymbol{\theta}}(\mathbf{V})\right\} \quad (15)$$

where $\nabla_{\boldsymbol{\theta}}$ is a column gradient operator with respect to $\boldsymbol{\theta}$. The Cramer-Rao bound states that for a unbiased estimator $\hat{\boldsymbol{\theta}}(\mathbf{V})$ for $\boldsymbol{\theta}$ from $\mathbf{V}$, the inverse Fisher information matrix provides a lower bound for the covariance of the estimator or

$$\mathrm{Cov}(\hat{\boldsymbol{\theta}}(\mathbf{V})) \geq \mathbf{J}(\mathbf{V}; \boldsymbol{\theta})^{-1}. \quad (16)$$

Thus, comparing Fisher information matrices of SSR-N, SSR-WA, and JSR can suggest their theoretical performance limits and relationships.

Assuming that SSR-N uses the first energy window $e = 1$, the Fisher information matrix for SSR-N with the measurement model (1) can be derived as

$$\mathbf{J}_{\mathrm{SSR-N}}(\mathbf{Y}_1; \mathbf{x}) = \tau_1 \mathbf{A}_1' \mathbf{D}\left(\frac{1}{\mathbf{A}_1\tau_1\mathbf{x} + \mathbf{s}_1}\right)\mathbf{A}_1\tau_1 \quad (17)$$

where $\mathbf{Y}_e$ is a random vector to generate a realization $\mathbf{y}_e$ in (1) and $\mathbf{x}$ is a ground truth image. The Fisher information matrix for SSR-WA in (13) can also be derived as

$$\mathbf{J}_{\mathrm{SSR-WA}}\left(\textstyle\sum_e \mathbf{Y}_e; \mathbf{x}\right) = \mathbf{A}_S' \mathbf{D}\left(\frac{1}{\mathbf{A}_S\mathbf{x} + \mathbf{s}_W}\right)\mathbf{A}_S \quad (18)$$

where $\mathbf{A}_S = \sum_e \mathbf{A}_e\tau_e$ and $\mathbf{s}_W = \sum_e \mathbf{s}_e$. The Fisher information matrix for JSR with the measurement model (8) can be obtained as

$$\mathbf{J}_{\mathrm{JSR}}(\mathbf{Y}_J; \mathbf{x}) = \mathbf{A}_J' \mathbf{D}\left(\frac{1}{\mathbf{A}_J\mathbf{x} + \mathbf{s}_J}\right)\mathbf{A}_J \quad (19)$$

where $\mathbf{Y}_J$ is a random vector to generate the realization $\mathbf{y}_J$ in (1) and $\mathbf{D}(\cdot)$ is a diagonal matrix with the elements in $(\cdot)$. Equation (19) simplifies to

$$\sum_e \tau_e \mathbf{A}_e' \mathbf{D}\left(\frac{1}{\mathbf{A}_e\tau_e\mathbf{x} + \mathbf{s}_e}\right)\mathbf{A}_e\tau_e. \quad (20)$$

For the random vector $\mathbf{V}$ and a multivariate function $\phi(\cdot)$, a data processing inequality holds for the Fisher information matrix as the following lemma:

Lemma 1 (Data Processing Inequality [19]):

$$\mathbf{J}(\mathbf{V}; \boldsymbol{\theta}) \geq \mathbf{J}(\phi(\mathbf{V}); \boldsymbol{\theta})$$

with equality if $\phi(\mathbf{V})$ is a sufficient statistic relative to the family $\{f_{\boldsymbol{\theta}}(\mathbf{v})\}$ (e.g., when $\phi(\cdot)$ is an invertible function).

The following propositions are true due to Lemma 1:

Proposition 1 (JSR vs. SSR-N):

$$\mathbf{J}_{\mathrm{JSR}}(\mathbf{Y}_J; \mathbf{x}) > \mathbf{J}_{\mathrm{SSR-N}}(\mathbf{Y}_1; \mathbf{x}). \quad (21)$$

Proof: $\mathbf{Y}_1 = [\mathbf{I}\ \mathbf{0}a \cdots\ \mathbf{0}]\mathbf{Y}_J$ and $[\mathbf{I}\ \mathbf{0}\ \cdots\ \mathbf{0}]$ is not invertible due to large null space from $\mathbf{0}$. Applying Lemma 1 with this non-invertible linear function proves the claim. ■

Proposition 2 (JSR vs. SSR-WA):

$$\mathbf{J}_{\mathrm{JSR}}(\mathbf{Y}_J; \mathbf{x}) > \mathbf{J}_{\mathrm{SSR-WA}}\left(\textstyle\sum_e \mathbf{Y}_e; \mathbf{x}\right). \quad (22)$$

Proof: $\sum_e \mathbf{Y}_e = [\mathbf{I}\ \mathbf{I}\ \cdots\ \mathbf{I}]\mathbf{Y}_J$ and $[\mathbf{I}\ \mathbf{I}\ \cdots\ \mathbf{I}]$ is not invertible due to large null space from multiple $\mathbf{I}$. Applying Lemma 1 with this non-invertible linear function proves the claim. ■

Therefore, an unbiased and efficient estimator for $\mathbf{x}$ using JSR should yield approximately and asymptotically the best performance in terms of covariance (precision) among all other unbiased (and efficient) estimators of SSR-N and SSR-WA since ML-EM is asymptotically unbiased and efficient. Therefore, our proposed JSR has favorable statistical properties over conventional SSR-N and recent SSR-WA in theory.

V. Monte-Carlo Simulation Results

A. MC Simulation and Reconstruction Setup

We performed a MC simulation using SIMIND [12] with a digital phantom ($128 \times 128 \times 128$ voxels with $4.8 \times 4.8 \times 4.8\mathrm{mm}^3$ per voxel) similar to the NEMA PET phantom [20], but with the 6 hot spheres expanded in volumes with the diameters of 1.5, 1.9, 2.4, 3.1, 3.7, 5.7 cm (about 2-100 mL). These diameters are more reasonable for SPECT considering spatial resolution and our Y-90 radioembolization dosimetry study with 22 patients (89 lesions) [21] in which the median lesion volume was 12 mL (range 2-58 mL) for hepatocellular carcinoma and 9 mL (range 2-828 mL) for liver metastases. The cylindrical lung insert of the NEMA phantom was unchanged. The activity concentration ratio between hot spheres, cold lung insert and background was 8:0:1. The hot-sphere to background activity concentration ratio was higher than the median value of 4:1 that we reported for the lesion-to-nontumoral liver activity concentration ratio in patients, but the ratio extended up to 39 [21], hence our value of 8 is clinically relevant.

SIMIND MC simulation for Siemens Intevo with high energy collimators was done with the 6 acquisition energy windows as shown in Fig. 1. Note that our SIMIND MC simulation used a new bremsstrahlung emission spectrum with both internal (IB) and external bremsstrahlung (EB) components of the spectrum and also accounted for beta range effects [22]. We selected these windows since the primary to scatter ratio drops off rapidly with energy and it is desirable to avoid x-ray and high order scatter at low energies. Using MC simulated projection data, a Poisson realization was obtained assuming 100 million detected counts for 105-195 keV range. 100 million counts were selected considering a typical total count of 10-20 million for our 30-min Y-90 SPECT patient

scans and 10 × larger simulated phantom volume than patient liver (typically 1000 mL) for similar count density.

Five reconstruction methods were performed as illustrated in Table I with up to 200 iterations and 4 ordered-subsets. For JSR-ES, additional 3 energy-subsets were used as proposed (12 subsets total). Gaussian kernel based CDR compensation and attenuation correction factor at the bremsstrahlung yield-weighted mean energy of each window were used in the forward projector. For the upper bound of 285 keV, additional modeling for CDR such as penetration tails [14] was not necessary. For scatter correction, the true scatter from MC simulation was used.

Additionally, we performed a multiple realization study to investigate our theoretical analysis results in Propositions 1 and 2. We reconstructed images from 25 Poisson measurement realizations and generated the mean and standard variation images over 25 images. we denote them by MEAN and STDEV images, respectively. These images are voxel-wise empirical mean and standard deviation.

B. Evaluation Criteria

Assuming that estimated emitted photon count is proportional to Y-90 activity, the calibration factor to convert counts to activity was determined using the total counts in the field of view and the known total activity. To define the target volumes, the true region outlines were used. Target counts were converted to activity by scaling with the calibration factor. We used the following metrics to assess the quantitative accuracy of all reconstruction methods: for hot spheres,

$$\mathrm{RC_{VOI}} = \frac{\text{mean of estimated activity in VOI}}{\text{mean of true activity in VOI}}$$

where RC, VOI stand for recovery coefficient, volume of interest, respectively. Average RC is a weighted average of RC values for all 6 hot spheres in the phantom with weights that are proportional to volumes of spheres. For cold sphere with 0 activity, the residual count error [20] was defined as

$$\mathrm{RCE_{VOI}} = \frac{\text{mean of estimated activity in VOI}}{\text{mean of estimated activity in BG}}$$

where BG stands for background VOI defined by the uniform region of the phantom background away from the spheres to avoid spill-out. As a measure of image noise, the coefficient of variation (CV) was used:

$$\mathrm{CV_{BG}} = \frac{\text{standard deviation of estimated activity in BG}}{\text{mean of estimated activity in BG}}.$$

Ideally, RC, RCE, and CV should be 1, 0, and 0, respectively.

For the multiple realization study, we introduced two metrics that may be able to better show the bias-variance tradeoff using the MEAN and STDEV images from multiple realizations. Similar metrics to RC were defined for the MEAN and STDEV image values as follows:

$$\mathrm{RCM_{VOI}} = \frac{\text{mean of MEAN image values in VOI}}{\text{mean of true activity in VOI}},$$

$$\mathrm{RCSD_{VOI}} = \frac{\text{mean of STDEV image values in VOI}}{\text{mean of true activity in VOI}}.$$

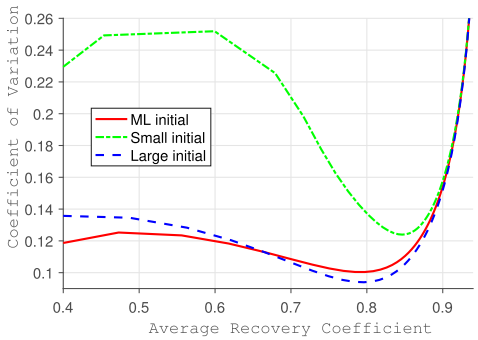

Fig. 2. CV for background vs. average RC for hot spheres for JSR with different initial images. Different initial images lead to different noise properties over average RC values.

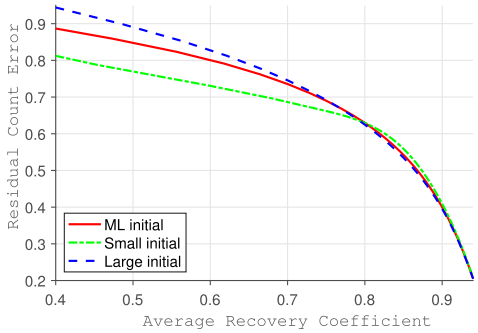

Fig. 3. RCE vs. average RC in the cold lung insert for JSR with different initial images.

RCM averages the voxel-wise mean values in VOI and RCSD averages the voxel-wise standard deviation values in VOI. These voxel-wise mean, standard deviation calculations should provide more accurate metrics for Propositions 1 and 2 that are also voxel-wise relationships.

C. Results for ML Based Initializations

Figs. 2 and 3 illustrate that choosing an appropriate initial image is important for good performance especially for the methods with early stopping. These figures were generated by calculating average RC, RCE, and CV of reconstructed images by changing the number of iterations for phantom simulations. Note that CV in background was high initially since it is normalized by low contrast and became high again later due to high noise in the later iteration of unregularized OSEM. "ML initial" implies that c in (11) is chosen based on (12). Let us denote this chosen value by c^*. "Small initial" and "Large initial" mean that relatively small $c \ll c^*$ and large $c \gg c^*$ are selected, respectively. It seems advantageous to use the ML optimal c^* for an initial image to obtain overall low CV in background and low RCE in the cold insert together over all average RCs. Even though only relatively high average RCs are concerned, our ML initialization can provide a nice lower-bound for c for low CV in background and low RCE in the cold insert. Note that these figures are the results for JSR, but similar tendency was also observed for SSR-N.

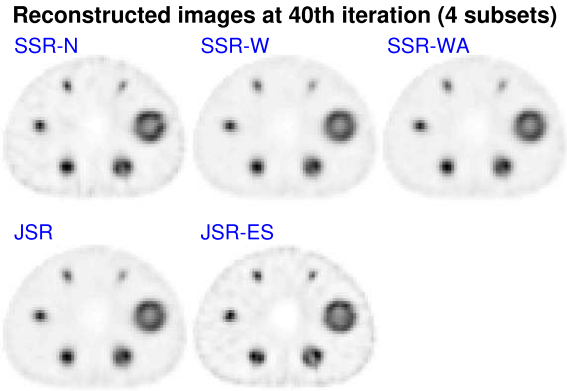

Fig. 4. Reconstructed images at the 40th iteration with 4 OS (SSR-N, SSR-W, SSR-WA, JSR) and 4 OS × 3 ES (JSR-ES).

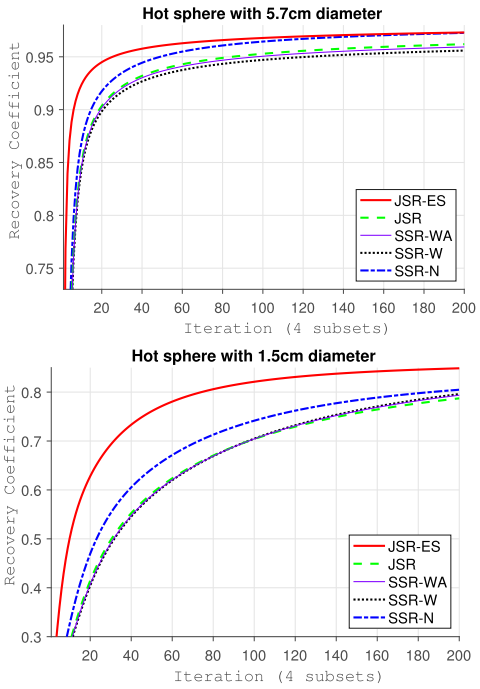

Fig. 5. RCs vs. iteration for two hot spheres with the diameters of 5.7 and 1.5 cm. Our proposed JSR-ES achieved higher RCs than other methods over iterations for all sphere volumes, especially for small spheres.

D. Results for JSR and JSR-ES

For phantom simulations, five reconstruction methods were applied as shown in Fig. 4. SSR-W, SSR-WA, and JSR yielded visually the most blurred images with low noise, while our proposed JSR-ES yielded the image with the highest contrast and highest noise. Fig. 5 shows RCs over iterations for two hot spheres. Our proposed JSR-ES achieved higher RCs than other methods over all iterations for all sphere volumes, especially for small spheres. If more iterations are run, these differences among RCs will become smaller for large hot spheres, but there are still significant RC difference for small spheres even after 200 iterations with 4 OS. Similarly, Fig. 6 shows RCE over iterations for all methods in the cold lung insert. Our proposed JSR-ES yielded the lowest value among all other methods. Thus, in terms of RC in hot spheres and RCE in cold

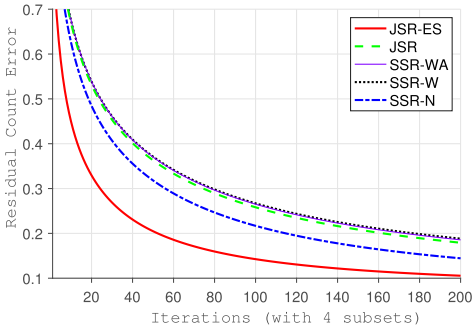

Fig. 6. RCE vs. iteration for the cold lung insert. Our proposed JSR-ES yielded the lowest RCE among all other methods.

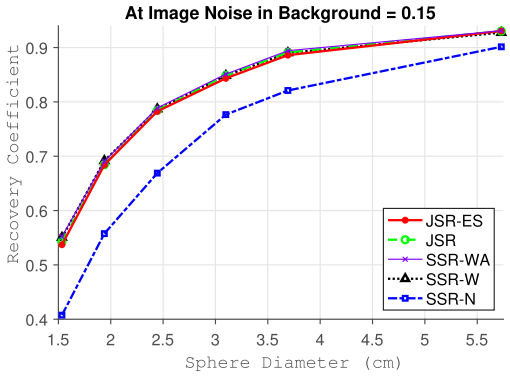

Fig. 7. RCs vs. sphere diameters at CV ≈ 0.15. All methods using all counts in the wide energy window yielded significantly better RC values than SSR-N using partial counts in the narrow energy window.

insert, our proposed JSR-ES yielded the fastest convergence rates over iterations among all methods.

Increased RC or decreased RCE often leads to increased noise level. Fig. 7 shows RCs over sphere volumes at CV ≈ 0.15. All methods using all counts in the wide energy window including our proposed methods yielded significantly better RC values than SSR-N using partial counts in the narrow energy window. This result clearly illustrates that using all counts is advantageous to achieve good RCs at similar noise level. Note that similar CV around 0.15 was achieved at the 12th (JSR-ES), 15th (SSR-N), 38th (JSR), and 41st (SSR-W, SSR-WA) iterations.

E. Results for Theoretical Comparisons

Fig. 8 shows the RCSD over background vs. the RCM over all 6 hot spheres (top) and the RCSD vs. the RCM over all hot spheres (bottom). Using all counts for JSR-ES, JSR, SSR-WA and SSR-W was one of the most important factors to achieve low noise level. JSR and JSR-ES yielded significantly lower noise level than SSR-N as shown in Proposition 1 and also yielded slightly lower noise than SSR-WA that is consistent with our Proposition 2 in both hot spheres and in background. Even though there was no theoretical comparison between JSR and SSR-W, we observed good performances of JSR and JSR-ES compared to SSR-W possibly due to less accurate forward model of SSR-W leading to poorer RCM at a given RCSD.

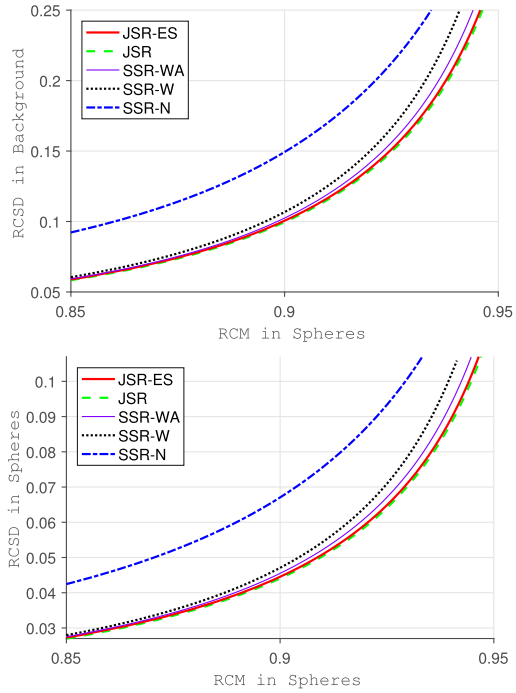

Fig. 8. RCSD in background vs. RCM in all 6 hot spheres (top) and RCSD vs. RCM in all hot spheres (bottom) that indirectly show bias-variance trade-off.

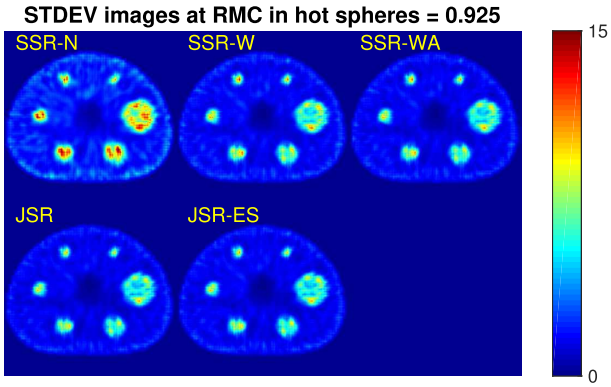

Fig. 9. A slice of the STDEV images at the iterations whose RCM in hot spheres = 0.925. All methods but SSR-N yielded similarly low STDEV images due to high counts. However, our proposed JSR, JSR-ES yielded slightly lower noise than SSR-W, SSR-WA near spheres.

The STDEV images at RCM in spheres $\approx$ 0.925 for different methods are illustrated in Fig. 9 showing consistent results as our Propositions 1 and 2. We were able to observe that SSR-N yielded the highest noise level among all methods. We also observed that JSR and JSR-ES yielded slightly lower noise levels than SSR-W and SSR-WA near small hot spheres.

VI. Experiment Results

A. Physical Phantom Experiment Setup

We also performed an experimental measurement with a physical elliptical-shaped phantom where the lengths of the long, short, longitudinal axes are 31, 22, 19 cm, respectively, with 6 hot spheres as shown in the bottom right sub-figure of Fig. 10 (1.6, 2, 2.5, 3.1, 3.8, 6 cm diameters) and 1 cold sphere that was located at the center of the phantom volume (5.7 cm diameter). The activity ratio between hot spheres, cold sphere, and background was approximately 9:0:1. Siemens Symbia SPECT-CT Intevo scanner with high energy collimator was used for data acquisition with the same 6 energy windows as our MC simulations in Section V-A. The total detected count for 105-195 keV energy range was about 8 million that was 12.5 times lower than the simulated counts in Section V-A.

SIMIND MC simulations were used to estimate scatter information for each window as described in [8]. Note that when generating the scatter estimate using SIMIND, we did not include the beta range effects because the input to the simulation is the measured SPECT activity distribution that has spatial resolution effects and the blurring due to resolution effects 'compensates' for the blurring due to beta range. For each scatter estimation update, 1.25 million histories $\times$ 12 cores $\times$ 2 hyper-threading were simulated with a SSR-N reconstructed image to generate common scatter information for all reconstruction methods and to save computation time (about 20 minutes per update). Initial input image to MC simulation was reconstructed by using SSR-N at 5 iteration (4 OS) without scatter information. Then, for the next 3 scatter updates, SSR-N reconstructed images at 5, 10, 15 iterations (4 OS) using previously estimated scatter information were used as inputs to MC simulations. Note that all reconstructions used the same ML based uniform image as an initial image. The last SIMIND MC simulation with a SSR-N reconstruction image at 15 iteration (4 OS) as an input image generated scatter information for all reconstruction methods and then all methods with this estimated scatter information were run with 20 iterations (4 OS $\times$ 3 ES for JSR-ES or 4 OS for others). We used our proposed ML based uniform initialization methods for all methods to yield better performance.

Inspired by our recent work [23], we implemented the following guided filter based denoising for noisy short-time MC scatter estimates for better performance. For the given measurement $\mathbf{y}_e$ and the SIMIND MC estimates $\mathbf{y}_{e,\mathrm{MC}}$, $\mathbf{s}_{e,\mathrm{MC}}$ at the eth energy window, the estimated scatter for SSR-N is

$$\hat{\mathbf{s}}_1 = \mathrm{GF}(\mathbf{s}_{1,\mathrm{MC}}; \tilde{\mathbf{y}}_{1,\mathrm{MC}}) \odot \mathrm{GF}(\mathbf{y}_1; \tilde{\mathbf{y}}_{1,\mathrm{MC}}) \oslash \tilde{\mathbf{y}}_{1,\mathrm{MC}}$$

where $\mathrm{GF}(\mathbf{b}; \mathbf{a})$ is the guided filter [24] with an input noisy image of $\mathbf{b}$ and a guide image $\mathbf{a}$ and $\tilde{\mathbf{y}}_{1,\mathrm{MC}} = \mathrm{GF}(\mathbf{y}_{1,\mathrm{MC}}; \mathbf{y}_{1,\mathrm{MC}})$. For other methods such as SSR-W, JSR, JSR-ES, since $\mathbf{y}_{W,\mathrm{MC}} = \sum_e \mathbf{y}_{e,\mathrm{MC}}$ is available, we obtained the scatter estimate as follows:

$$\hat{\mathbf{s}}_e = \mathrm{GF}(\mathbf{s}_{e,\mathrm{MC}}; \tilde{\mathbf{y}}_{W,\mathrm{MC}}) \odot \mathrm{GF}(\mathbf{y}_W; \tilde{\mathbf{y}}_{W,\mathrm{MC}}) \oslash \tilde{\mathbf{y}}_{W,\mathrm{MC}}$$

where $\tilde{\mathbf{y}}_{W,\mathrm{MC}} = \mathrm{GF}(\mathbf{y}_{W,\mathrm{MC}}; \mathbf{y}_{W,\mathrm{MC}})$.

The same evaluation metrics such as RC, RCE, and CV were used. To define the target volumes for the evaluation, outlines defined on CT were used in this experiment.

B. Results of Fast Convergence for Energy-Window Subset

For the phantom experiment, four reconstruction methods were applied as shown in Fig. 10. Our proposed JSR-ES yielded the highest contrasts for all hot spheres at the 20th

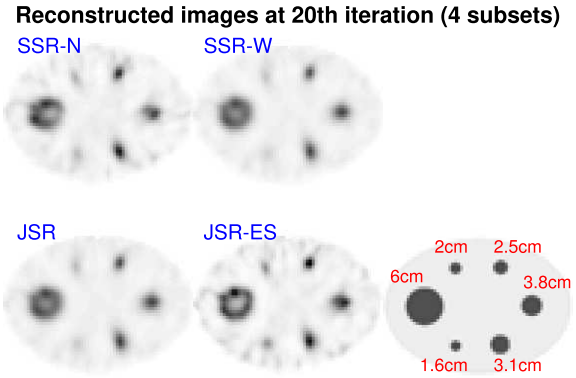

Fig. 10. Physical phantom reconstructed images at the 20th iteration using SSR-N, SSR-W, JSR (all 4 OS), and JSR-ES (4 OS × 3 ES). A diagram for the physical phantom with the diameters of all hot spheres is on bottom right.

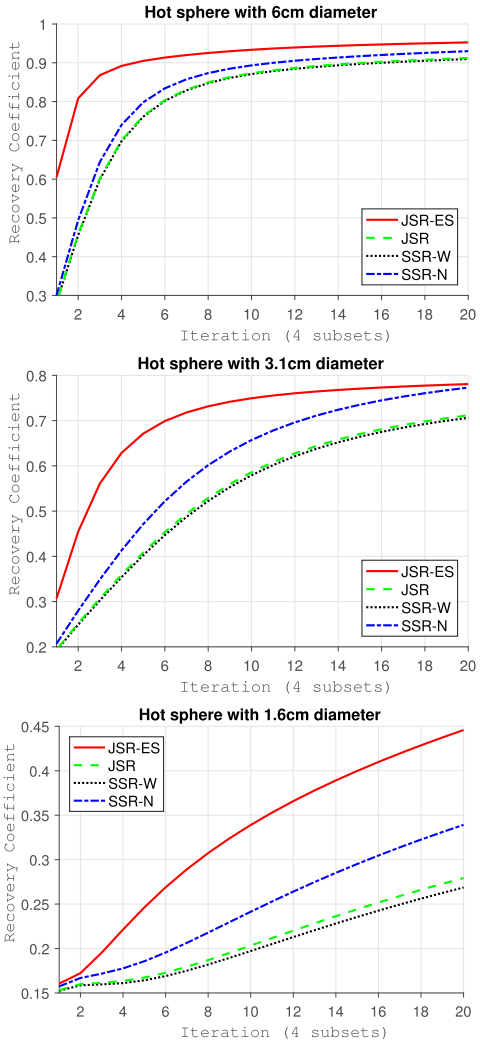

Fig. 11. RCs vs. iteration for 3 hot spheres. Our proposed JSR-ES yielded substantially higher RCs than all other methods over all iterations.

iteration, even for the smallest sphere with 1.6 cm diameter. Figs. 11 and 12 show RCs vs. iteration for 3 hot spheres and RCE vs. iteration for a cold sphere. Our proposed JSR-ES

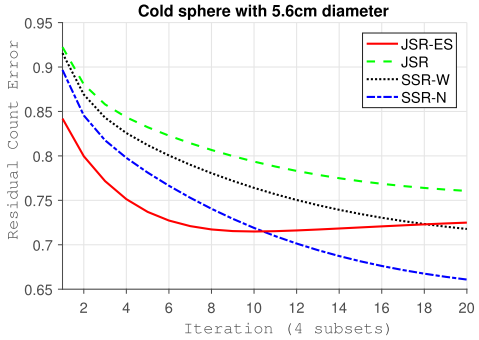

Fig. 12. RCE vs. iteration for the cold sphere. Our proposed JSR-ES yielded lower RCE than all other methods for early to mid iterations.

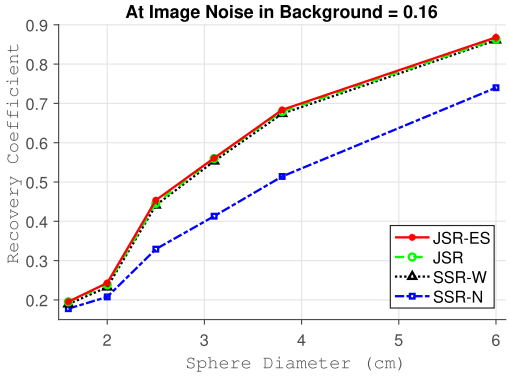

Fig. 13. RC vs. sphere diameter at CV = 0.16 for real phantom experiment.

yielded the highest RCs among all other methods over all sizes of sphere diameters, which are consistent with our digital phantom simulation results in Fig. 5. Our proposed JSR-ES also yielded lower RCE than all other methods for early to mid-iterations, which are consistent with our simulation results in Fig. 6. However, SSR-N yielded lower RCE than other methods after the 11th iteration.

Fig. 13 shows RCs vs. sphere diameters at CV = 0.16. All methods using the counts from the full range were able to yield similar RCs over sphere volumes, while SSR-N that used partial counts yielded much lower RCs than other methods including our proposed JSR and JSR-ES. Note that CV = 0.16 can not be exactly achieved since iterations are integers so that CV values over iterations are also discretized. CV ≈ 0.16 were achieved at the 4th (SSR-N), 9th (SSR-W, JSR) and 3rd (JSR-ES) iterations, respectively.

VII. Discussion

The continuous energy spectrum that extends to high energies and the relatively low bremsstrahlung yield makes quantitative Y-90 SPECT challenging. While previous state-of-the-art work to exploit this continuous energy spectrum [9], [11] relied on the SSR-WA model that has a single-band acquisition window with a wide energy range, our proposed JSR used multi-band acquisition windows. This difference in the forward model enabled us to prove better performance of our proposed JSR over the model of SSR-WA theoretically and empirically. It also enabled us to propose the ES

approximation for empirically fast convergence. Note that our proposed methods were not directly compared with the works of [9], [11]. SSR-WA is the model underlying [9] and [11] and the current work compares our proposed methods with the SSR-WA method whose model is almost equivalent to the models underlying [9], [11], rather than with the methods of [9], [11] themselves. There are trade-offs in computation complexity, ways of using MC runs, and accuracy of MC simulations that were not considered in our analyses. The work of [9] used pre-calculated scatter kernel values from MC simulations for both $\mathbf{A}_S$ and $\mathbf{s}_W$, while the work of [11] performed MC simulations for both $\mathbf{A}_S$ and $\mathbf{s}_W$ every iteration. In our implementation, we followed the MC scatter estimation of [8] to generate $\mathbf{s}_W = \sum_e \mathbf{s}_e$ every 5 iterations using SIMIND that included full radiation transport physics in the collimator, but the work of [11] made approximations for the collimator so that the simulation time could be reduced by using pre-calculated kernels instead of accurately modeling collimator interactions that is one of the most time-consuming parts of the MC run. Assuming the same MC simulator used, our method will hypothetically be less computationally intensive than the approach of [11] without giving up matched backward projectors in calculating both $\mathbf{a}_S$ and $\nabla \mathrm{L}(\cdot)$.

In this work, some performance comparisons of different methods such as RC or RCE were done over iterations, not over computation time. Fair comparison over computation time is challenging due to many computation factors and different implementations. For example, our current implementation computes each forward model for each narrow band. JSR, JSR-ES and SSR-WA require nearly the same computation time per iteration and they also require $\sim$6 times more computation time than SSR-N and SSR-W. Our current implementation seems suboptimal considering the fact that common computation among different energy bands could be shared such as line-of-response evaluation. Another factor to consider is heavy computation time for MC scatter estimation updates that usually take much more time than one forward projection. For MC simulation based forward model in the work of [11], optimal number of histories should be considered for fair comparisons. Therefore, further investigation is necessary for fair comparisons over computation time.

Direct comparison between our proposed methods and MC-based reconstructions [11] is challenging. MC-based reconstructions have an advantage of using more accurate forward models over our proposed methods. However, they typically use unmatched projectors while our proposed methods can use matched projectors for nice convergence properties that could be critical for unregularized algorithms for high contrast recovery and regularized reconstruction methods with advanced image priors. Often, these unmatched operators are not favorable to use since they do not guarantee some of the desired statistical properties of ML-EM such as asymptotic unbiasedness and efficiency of estimators. Furthermore, our JSR methods are not as computationally demanding as MC methods since our reconstructions use MC only to generate the scatter estimate, which is only updated 2-3 times [8] instead of at each iteration, and requires fewer histories than full MC.

We used hot sphere to background activity concentration ratios that were clinically relevant. However, in the experimental measurements it is logistically difficult to use a phantom with the same activity concentration levels as in a patient because these patients are administered $\sim$100 mCi to the liver. To be specific, our physical phantom experiment acquired 8 million counts in the 105-195 keV energy window that was similar to that of a patient study, but the activity is distributed in the large phantom (not focal liver activity as in patients), thus the activity concentration levels in our experimental study with 8 million counts and our MC simulation with 100 million counts in the energy window of 105-195 keV are quite different. Despite different imaging conditions, we found that the results for the physical phantom experiment are consistent with the results for the digital phantom simulation in most cases such as RCs of hot spheres and CV in background. Therefore, one can expect that the findings hold in clinical imaging conditions with parameters in between the two "extremes." At the 20th iteration, JSR-ES yielded 31.4% and 65.9% better RCs than SSR-N and SSR-W, respectively, for the smallest hot sphere. However, we found some inconsistencies for RCE in cold regions over relatively high iterations. There are a couple of possible explanations such as inaccurate or challenging scatter estimation for Y-90 reconstruction, or challenging reconstruction in zero activity areas due to the non-negativity constraint in image domain [25]. This phenomenon is expected to be more severe in JSR than SSR due to the small number of primary counts in high energy windows.

The cold center artifact in Figs. 4 and 10 is the result of resolution modeling in ML reconstruction, which can lead to significant artifacts (Gibbs phenomenon). This effect was first described by Snyder *et al.* [26] and a detailed discussion and an example image is included in the paper by Rahmim *et al.* [27]. They are severe in large spheres as used in our study (about 100 mL for the largest sphere) while there is no edge artifact in small spheres. We previously showed that regularized reconstruction with CT side information is one solution to this problem [28].

The JSR methods developed here were evaluated for the 105 to 285 keV, but can be applied to a wider range. Extending to higher energies may not lead to a substantial gain in primary counts (Fig. 1), but extending to lower energies will increase primary counts, potentially without degradation in quantitative accuracy. For example, a previous study investigated single windows in the range 70-410 keV and found the 90-125 keV window gave the best results [7]. The JSR methods developed here can also be applied to other beta emitters that rely on bremsstrahlung photons for SPECT, such as P-32. Furthermore, the methods can be applied to radionuclides that have multiple gamma-ray emissions with low yield, such as Lu-177, that can benefit from utilizing multiple windows to capture all the information to increase counts in contrast to standard reconstruction that uses only one of the gamma-rays.

Lastly, we used the Fisher information in our theoretical analyses and RC, RCE, and CV in our simulation and experiment for assessing overall image fidelity. While these metrics seem useful for dose-outcome evaluation [29], there are other metrics such as lesion-detection task based assessment,

non-uniform 3-D dosimetry or dose-volume histogram [30]. Further investigations of our proposed methods on these metrics can be interesting future works.

VIII. Conclusion

We proposed JSR, a novel Y-90 SPECT reconstruction method that uses a wide energy spectrum with accurate forward modeling. We theoretically and empirically showed that our JSR with multi-band forward model and multi-acquisition windows has favorable statistical properties over other competing methods with multi-band forward model and single acquisition window, and with single-band forward model and single acquisition window. We also proposed an ES approximation algorithm for JSR to yield faster empirical convergence in most cases for both MC simulation and experimental study except for the RCE on a cold sphere at high iterations in experimental study when using estimated scatter. Our ML-based initial image optimization for all methods yielded better performance in early iterations.

References

[1] R. Lhommel *et al.*, "Feasibility of ^{90}Y TOF PET-based dosimetry in liver metastasis therapy using SIR-spheres," *Eur. J. Nucl. Med. Mol. Imag.*, vol. 37, no. 9, pp. 1654–1662, Apr. 2010.

[2] A. Kennedy, "Radioembolization of hepatic tumors," *J. Gastrointestinal Oncol.*, vol. 5, no. 3, pp. 178–189, Jun. 2014.

[3] S. J. Goldsmith, "Radioimmunotherapy of lymphoma: Bexxar and Zevalin," *Seminars Nucl. Med.*, vol. 40, no. 2, pp. 122–135, Mar. 2010.

[4] J. J. Zaknun *et al.* "The joint IAEA, EANM, and SNMMI practical guidance on peptide receptor radionuclide therapy (PRRNT) in neuroendocrine tumours," *Eur. J. Nucl. Med. Mol. Imag.*, vol. 40, no. 5, pp. 800–816, May 2013.

[5] D. Minarik, K. S. Gleisner, and M. Ljungberg, "Evaluation of quantitative ^{90}Y SPECT based on experimental phantom studies," *Phys. Med. Biol.*, vol. 53, no. 20, pp. 5689–5703, Sep. 2008.

[6] C. F. Uribe, P. L. Esquinas, M. Gonzalez, and A. Celler, "Characteristics of Bremsstrahlung emissions of ^{177}Lu, ^{188}Re, and ^{90}Y for SPECT/CT quantification in radionuclide therapy," *Phys. Med.*, vol. 32, no. 5, pp. 691–700, May 2016.

[7] W. Siman, J. K. Mikell, and S. C. Kappadath, "Practical reconstruction protocol for quantitative ^{90}Y bremsstrahlung SPECT/CT," *Med. Phys.*, vol. 43, no. 9, pp. 5093–5103, Aug. 2016.

[8] Y. K. Dewaraja *et al.*, "Improved quantitative ^{90}Y bremsstrahlung SPECT/CT reconstruction with Monte Carlo scatter modeling," *Med. Phys.*, vol. 44, no. 12, pp. 6364–6376, Dec. 2017.

[9] X. Rong, Y. Du, M. Ljungberg, E. Rault, S. Vandenberghe, and E. C. Frey, "Development and evaluation of an improved quantitative ^{90}Y bremsstrahlung SPECT method," *Med. Phys.*, vol. 39, no. 5, pp. 2346–2358, 2012.

[10] J. Yue *et al.*, "Comparison of quantitative Y-90 SPECT and non-time-of-flight PET imaging in post-therapy radioembolization of liver cancer," *Med. Phys.*, vol. 43, no. 10, pp. 5779–5790, Oct. 2016.

[11] M. Elschot, M. G. E. H. Lam, M. A. A. J. van den Bosch, M. A. Viergever, and H. W. A. M. de Jong, "Quantitative Monte Carlo–based ^{90}Y SPECT reconstruction," *J. Nucl. Med.*, vol. 54, no. 9, pp. 1557–1563, Sep. 2013.

[12] M. Ljungberg, "The SIMIND Monte Carlo program," in *Monte Carlo Calculations in Nuclear Medicine*, M. Ljungberg, S.-E. Strand, and M. A. King, Eds. Boca Raton, FL, USA: CRC Press, 2012, pp. 111–128.

[13] M. P. Nguyen, H. Kim, S. Y. Chun, J. A. Fessler, and Y. K. Dewaraja, "Joint spectral image reconstruction for Y-90 SPECT with multi-window acquisition," in *Proc. IEEE Nucl. Sci. Symp. Med. Imag. Conf.*, Oct./Nov. 2015, pp. 1–4.

[14] S. Y. Chun, J. A. Fessler, and Y. K. Dewaraja, "Correction for collimator-detector response in SPECT using point spread function template," *IEEE Trans. Med. Imag.*, vol. 32, no. 2, pp. 295–305, Feb. 2013.

[15] L. A. Shepp and Y. Vardi, "Maximum likelihood reconstruction for emission tomography," *IEEE Trans. Med. Imag.*, vol. MI-1, no. 2, pp. 113–122, Oct. 1982.

[16] H. M. Hudson and R. S. Larkin, "Accelerated image reconstruction using ordered subsets of projection data," *IEEE Trans. Med. Imag.*, vol. 13, no. 4, pp. 601–609, Dec. 1994.

[17] S. Y. Chun, H. Lim, J. A. Fessler, and Y. K. Dewaraja, "On parameter selection for joint spectral reconstruction in Y90 SPECT," in *Proc. IEEE Nucl. Sci. Symp. Med. Imag. Conf.*, Nov. 2018, pp. 1–4.

[18] M. Elschot, B. J. Vermolen, M. G. E. H. Lam, B. de Keizer, M. A. A. J. van den Bosch, and H. W. A. M. de Jong, "Quantitative comparison of PET and Bremsstrahlung SPECT for imaging the *in vivo* yttrium-90 microsphere distribution after liver radioembolization," *PLoS ONE*, vol. 8, no. 2, Feb. 2013, Art. no. e55742.

[19] R. Zamir, "A proof of the Fisher information inequality via a data processing argument," *IEEE Trans. Inf. Theory*, vol. 44, no. 3, pp. 1246–1250, May 1998.

[20] M. E. Daube-Witherspoon *et al.*, "PET performance measurements using the NEMA NU 2-2001 standard," *J. Nucl. Med.*, vol. 43, no. 10, pp. 1398–1409, Oct. 2002.

[21] Y. K. Dewaraja *et al.*, "Prediction of tumor control in ^{90}Y radioembolization by logit models with PET/CT based dose metrics," *J. Nucl. Med.*, early access, May 2019, doi: 10.2967/jnumed.119.226472.

[22] Y. Dewaraja, R. Fleming, P. Simpson, S. Walrand, M. Ljungberg, and S. Wilderman, "Impact of internal bremsstrahlung on Y-90 SPECT imaging," *J. Nucl. Med.*, vol. 59, no. 1, p. 577, May 2018.

[23] H. Kim, S. Y. Chun, J. A. Fessler, and Y. K. Dewaraja, "On enhancing Monte-Carlo scatter correction for Y90 bremsstrahlung SPECT using guided filtering," *J. Nucl. Med.*, vol. 59, no. 1, p. 1348, Jun. 2019.

[24] K. He, J. Sun, and X. Tang, "Guided image filtering," *IEEE Trans. Pattern Anal. Mach. Intell.*, vol. 35, no. 6, pp. 1397–1409, Jun. 2013.

[25] H. Lim, Y. K. Dewaraja, and J. A. Fessler, "A PET reconstruction formulation that enforces non-negativity in projection space for bias reduction in Y-90 imaging," *Phys. Med. Biol.*, vol. 63, no. 3, Feb. 2018, Art. no. 035042.

[26] D. L. Snyder, M. I. Miller, L. J. Thomas, and D. G. Politte, "Noise and edge artifacts in maximum-likelihood reconstructions for emission tomography," *IEEE Trans. Med. Imag.*, vol. MI-6, no. 3, pp. 228–238, Sep. 1987.

[27] A. Rahmim, J. Qi, and V. Sossi, "Resolution modeling in PET imaging: Theory, practice, benefits, and pitfalls," *Med. Phys.*, vol. 40, no. 6, p. 064301, 2013.

[28] Y. K. Dewaraja, K. F. Koral, and J. A. Fessler, "Regularized reconstruction in quantitative SPECT using CT side information from hybrid imaging," *Phys. Med. Biol.*, vol. 55, no. 9, pp. 2523–2529, May 2010.

[29] C. Chiesa *et al.*, "Radioembolization of hepatocarcinoma with ^{90}Y glass microspheres: Development of an individualized treatment planning strategy based on dosimetry and radiobiology," *Eur. J. Nucl. Med. Mol. Imag.*, vol. 42, no. 11, pp. 1718–1738, Oct. 2015.

[30] W. Siman, J. K. Mikell, O. R. Mawlawi, F. Mourtada, and S. C. Kappadath, "Dose volume histogram-based optimization of image reconstruction parameters for quantitative ^{90}Y-PET imaging," *Med. Phys.*, vol. 46, no. 1, pp. 229–237, 2019.